Research Article Vol. 30, No. 2 / 17 Jan 2022 / Optics Express 1381

Optics EXPRESS

Second and cascaded harmonic generation of pulsed laser in a lithium niobate on insulator ridge waveguide

CHUANYI LU,[1] HAO LI,[1] JING QIU,[2] YUTING ZHANG,[1] SHIJIE LIU,[1,5] YUANLIN ZHENG,[1,3,6] AND XIANFENG CHEN[1,2,3,4,7]

[1] *State Key Laboratory of Advanced Optical Communication Systems and Networks, School of Physics and Astronomy, Shanghai Jiao Tong University, Shanghai 200240, China*
[2] *Jinan Institute of Quantum Technology, Jinan 250101, China*
[3] *Shanghai Research Center for Quantum Sciences, Shanghai 201315, China*
[4] *Collaborative Innovation Center of Light Manipulations and Applications, Shandong Normal University, Jinan 250358, China*
[5] *liushijie@sjtu.edu.cn*
[6] *ylzheng@sjtu.edu.cn*
[7] *xfchen@sjtu.edu.cn*

Abstract: Nonlinear crystalline ridge waveguides, e.g., lithium niobate-on-insulator ridge waveguides, feature high index contrast and strong optical confinement, thus dramatically enhancing nonlinear interaction and facilitating various nonlinear effects. Here, we experimentally demonstrate efficient second-harmonic generation (SHG) and cascaded fourth-harmonic generation (FHG) in a periodically poled lithium niobate (PPLN) ridge waveguide pumped with pulsed laser at the quasi-phase matching (QPM) wavelength, as well as simultaneous SHG and cascaded third-harmonic generation (THG) waves when pumped at the non-QPM wavelength. Furthermore, the ridge waveguide achieves an efficient single-pass SHG conversion efficiency of picosecond pulsed laser at ~62%. These results may be beneficial for on-chip nonlinear frequency conversion.

1. Introduction

Integrated photonics holds great potential for communication, signal processing and quantum network applications [1,2]. Lithium niobate is one of the most versatile and popular photonic material, due to its wide transparent window (0.4-5 μm), excellent electro-optic property and strong second-order nonlinearity. Recently, with breakthroughs in microfabrication techniques, lithium niobate-on-insulator (LNOI) has emerged as a competitive and promising candidate for integrated (nonlinear) photonics platform [3–5]. Thus far, various important functions have been developed on the LNOI platform, including high-performance modulators [6–9], acousto-optic devices [10], efficient nonlinear wavelength converters [11–13] and photon-pair sources [14,15]. Among them, there are several essential components of integrated photonics, such as ridge waveguides [13–18], photonic crystal cavities [19,20], microdisks [21,22] and microrings [23,24].

Optical waveguides, with strong light confinement, are preferred in integrated photonics. However, conventional waveguides, fabricated either with titanium (Ti) in-diffusion or with proton exchange, suffer from low index contrast ($\Delta n \sim 0.02$) between the core and cladding, resulting in large bending radii and large device dimensions, making it challenging for dense integration. These restrictions can be addressed by using LNOI ridge waveguides with much higher index contrast ($\Delta n \sim 0.7$) and stronger optical confinement, which can dramatically enhance nonlinear interactions. Combined with the flexibility in ferroelectric domain reverse, they can achieve ultrahigh conversion efficiencies (~2600%$\mathrm{W}^{-1}\mathrm{cm}^{-2}$ for SHG at 1550 nm [13])

#447958 https://doi.org/10.1364/OE.447958
Journal © 2022 Received 7 Nov 2021; revised 18 Dec 2021; accepted 20 Dec 2021; published 4 Jan 2022

Optics EXPRESS

which are inaccessible in their bulk counterparts or conventional waveguides (~90%$W^{-1}cm^{-2}$ for SHG at 1550 nm in reversed-proton exchange waveguide). However, the output power is restricted due to the small mode field diameter (MFD) of the nanowaveguides and special coupling design is required. The difficulty can be mitigated by using microscale waveguides with large MFD [25,26]. As for nonlinear photonics applications, the goal is to realize high conversion efficiency with high-power continuous-wave laser or pulsed laser at single pass [27], which holds great promise in wavelength conversion and all-optical single processing in optical communication systems. The most feasible approach is the ridge waveguide with large MFD in view of high damage threshold. Recently, the overall SHG conversion efficiency up to 58% is successfully demonstrated at 1550 nm [28]. Besides, large MFD can be efficiently coupled to standard single-mode optical fiber without special design, which is favorable in scalable fabrication and real communication applications.

Cascaded second-order nonlinear processes can induce a large effective Kerr nonlinearity, which could tremendously reduce the pump power as compared with a direct third-order process [29,30]. The emergence and rapid development of the LNOI technology enable various on-chip devices with unprecedented performances. Cascaded second-order processes will inject new vitality and provide exciting possibilities in nonlinear dynamics on the LNOI platform. In LNOI microdisks, cascaded second-order processes, such as second-/third-harmonic generation (SHG or THG) [21,31] and effective four-wave mixing [32], have been reported for a variety of applications. The cascaded electro-optic effect and second-order frequency conversion have been demonstrated in the LNOI ridge waveguide which offers a method of electrically controlling nonlinear conversion [33]. Besides, the multi-octave spanning supercontinuum spectrum in PPLN nanowaveguides [34] and high harmonic generation (up to the 13th harmonic) in a chirped PPLN ridge waveguide [35] have also been realized through a chain of successive cascaded processes.

In this work, we demonstrate efficient second to fourth harmonic generation in a single PPLN ridge waveguide on the LNOI platform pumped by short pulsed laser. Besides, we report a high single-pass SHG conversion efficiency (~62%) of picosecond pulsed laser in the pump-depletion region, which provides a method to realize high-efficiency frequency conversion.

2. Experiment and results

The PPLN ridge waveguide has a dimension of 10 μm (W) $\times$ 5 $\mu m\,(H) \times 20mm\,(L)$. It is fabricated with a z-cut LNOI wafer, which consists of a 5-µm-thick crystalline lithium niobate on top of a 2-µm-thick buried silica buffering layer above a silicon substrate. Periodical poling of the LNOI is performed using an electrical field poling technique. The poling period, Λ, of the waveguide is approximately 18 µm with a duty cycle of (36 ± 1)%, which takes into consideration both the material and waveguide dispersion. Then, the ridge structure of the LNOI waveguide is formed between two parallel grooves with a depth of ~2.5 µm in the chip by optical grade dicing. For the PPLN ridge waveguide, the QPM grating provides a reciprocal lattice vector (RLV) k_{QPM} to compensate the phase mismatch during the nonlinear coupling process in the waveguide, with $k_{QPM} = 2\pi m/\Lambda$ and m being the QPM order. The type-0 phase matching scheme is employed to achieve high conversion efficiency. In the z-cut configuration, the transverse-magnetic (TM) polarized modes access the highest second-order nonlinear coefficient d_{33} (~27 pm/V). Figures 1(a) and 1(b) depict the numerically simulated fundamental TM_{00} mode profiles at the fundamental (~1556.22 nm) and SH (~778.11 nm) wavelengths, respectively.

Firstly, normalized SHG conversion efficiency using continuous-wave (cw) pump is experimentally measured to evaluate the performance of the PPLN ridge waveguide. Light from a cw tunable telecom-band laser (1520-1600 nm) is amplified by an erbium-doped fiber amplifier (EDFA). The pump whose polarization is controlled by a polarization controller (PC) enters the ridge waveguide through an end-coupling setup. Two single-mode fiber pigtails couple

Optics EXPRESS

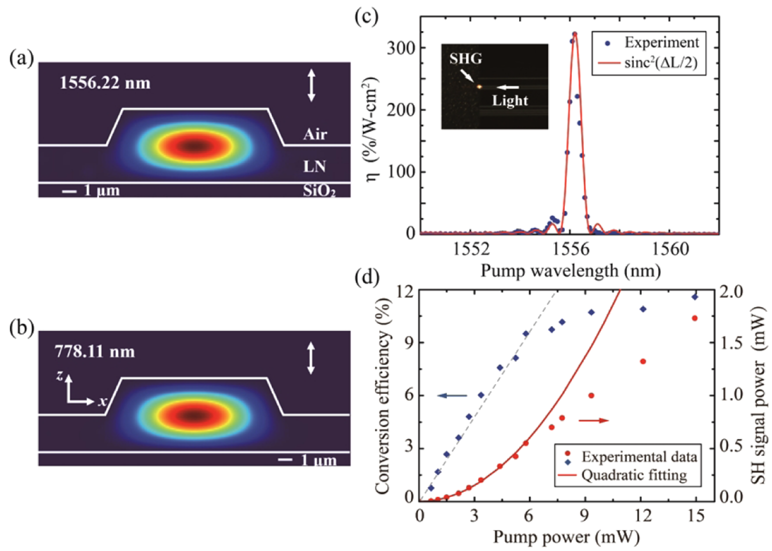

Fig. 1. (a) and (b) Simulation of the fundamental TM mode profiles at the fundamental (1556.22 nm) and SH wavelength (778.11 nm) in the ridge waveguide, respectively. The arrows in the upper right corner denote the direction of polarization. (c) Measured SHG efficiency versus the pump wavelength at room temperature. Inset: top-view of scattered SHG light at the output end. (d) SHG power (red) and conversion efficiency (blue) as a function of input pump power.

the light in and out of the PPLN ridge waveguide. At the output end, the pump and SH light are separated by a 780/1550 wavelength-division multiplexer (WDM) with a 60-dB isolation ratio, then monitored by an optical spectrum analyzer (OSA) as well as a power meter. The normalized SHG conversion efficiency is defined as $P_{SH}/(P_P^2 \cdot L^2)$ [13], where P_P and P_{SH} are the powers of the fundamental wave and generated SH wave measured at the output, L is the interaction length. The measured total fiber-chip-fiber transmission of the PPLN waveguide is ∼40% and the propagation loss is 0.8 dB/cm at around 1550 nm by using the Fabry-Perot interference method, comparable to other reports [36,37]. The measured SHG efficiency with respect to the pump wavelength is shown in Fig. 1(c). As shown in the inset, scattered SH light at the output facet is observed when the pump is set to the QPM wavelength of 1556.22 nm. The measured efficiency spectrum is well consistent with the theoretical modelling. The peak normalized SHG efficiency is ∼320%$W^{-1}cm^{-2}$ with a QPM bandwidth of about 0.5 nm. This is relatively high for micrometer PPLN ridge waveguides [28,36,37]. The measured conversion efficiency can be improved by using 50% poling duty, but this would eliminate further cascading processes as will be discussed later. The measured SH power and conversion efficiency is plotted in Fig. 1(d). The SH power follows a quadratic response on the pump in the low-conversion limit. When the input power is increased to ∼6 mW, SHG tends to saturate. The measured highest single-pass conversion efficiency is 11.6% with a generated SH power of 1.74 mW at a pump power of 15 mW. The saturation may be due to the photorefractive effect of lithium niobate, which can be circumvented by magnesium doping.

For short pulsed laser input, we utilize a mode-locked pulsed optical fiber laser as the pump source. The laser produces 500 fs-long-pulses centered at 1556 nm at a 60-MHz repetition rate. The laser has a spectral bandwidth of approximately 10 nm. When directly pumped by the femtosecond laser, multiple colored emission is observed as shown in Fig. 2, which involves cascading processes. At the output end, the generated harmonic light is collimated by a long-focus lens and then dispersed by a prism. In Fig. 2(b), the ultraviolet harmonic manifests as a faint blue spot mainly due to the fluorescence of the paper screen. In addition, the output light signals cover three colors (red, green and purple). The discrete peaks are located at around 778, 519 and 389 nm, respectively corresponding to second, third and fourth harmonic generation.

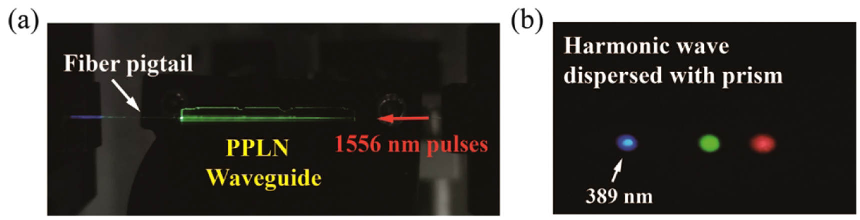

Fig. 2. (a) Image of the PPLN ridge waveguide when excited with 1556 nm femtosecond laser. (b) The generated cascaded harmonic light dispersed by a prism.

To investigate the cascaded mechanism of harmonics generation, a narrow tunable optical filter (its full width at half maximum bandwidth is 0.45 nm) is placed after the mode-locked pulse laser, to generate narrow bandwidth pulsed pump with tunable central wavelength. After the filter, the laser pulses are theoretically stretched to about 8 picoseconds (Gaussian pulse shape assumed). The PPLN ridge waveguide has the specific poling period to satisfy the first-order QPM condition for SHG. Efficient SHG (~778.11 nm) and FHG (~389.05 nm) are simultaneously observed when the central wavelength is turned to the QPM wavelength of 1556.22 nm. In this configuration, the FHG is created through the cascaded processes involving SHG ($\omega + \omega \rightarrow 2\omega$) and successive

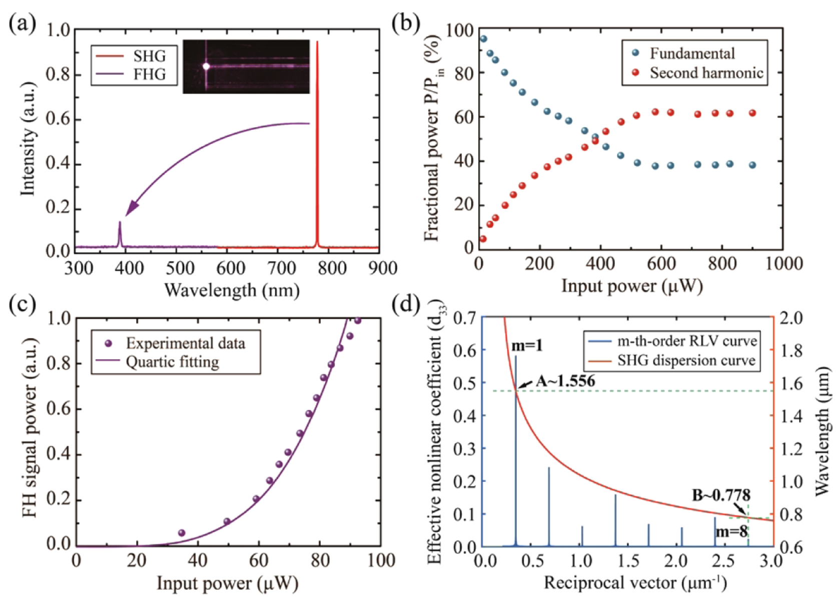

Fig. 3. SHG and cascaded FHG in PPLN waveguide pumped with pulsed laser at 1556.22 nm. (a) Measured spectrum of the SHG (~778.11 nm) and FHG (~389.05 nm) (not to scale). Inset: top-view of the waveguide. (b) Measured SHG conversion efficiency (red) and pump-depletion ratio (blue) as a function of input pulse power, showing 62% single-pass conversion efficiency with an input pulse power of 580 μW. (c) Measured FHG power versus the input power and the corresponding quartic fitting. (d) Calculated effective nonlinear coefficient and the SHG phase mismatching of the PPLN ridge waveguide.

Optics EXPRESS

SHG ($2\omega + 2\omega \rightarrow 4\omega$). The spectra of SHG and FHG are analyzed and plotted in Fig. 3(a). The inset displays a top view of the waveguide with scattered red and ultraviolet harmonics. The input pulse power is gradually changed to quantify the SHG conversion efficiency and pump-depletion ratio. As is shown in Fig. 3(b), SHG conversion efficiency saturates at moderate input pulse powers (~520 μW). The measured highest single-pass conversion efficiency is ~62% with an input pulse power of only ~580 μW in the pump-depletion region. As presented in Fig. 3(c), the FH signal has a fitted quartic dependence on the input power in the small signal condition as expected in the nonlinear conversion process.

To illustrate the mechanism of QPM for SHG and cascaded FHG in the PPLN ridge waveguide, the RLV of the PPLN waveguide is numerically calculated by making a Fourier transform of the domain inversion structure [29,30]. Figure 3(d) exhibits that the PPLN structure has a series of discrete RLVs with high effective nonlinear coefficients. Each RLV line satisfies a QPM condition for SHG at a specific fundamental wavelength. The non-zero effective nonlinear coefficients of even order QPMs result from the poling duty away from 50:50. The PPLN waveguide can support both first-order and higher-order QPM conversions. Furthermore, we calculate and plot the phase mismatching curve for SHG considering the effective refractive index in the PPLN waveguide. It is evident that the waveguide can achieve first-order QPM for SHG at around 1556 nm with SH wavelength at 778 nm (point A). An eight-order QPM SHG process occurs at approximately 778 nm (point B), which finally leads to the consequent cascaded FHG observed in the experiment.

When the input pulsed laser is scanned to the non-QPM wavelength of 1556.75 nm (still on the QPM condition but slightly away from the perfect point), efficient SH (~778.37 nm) and cascaded

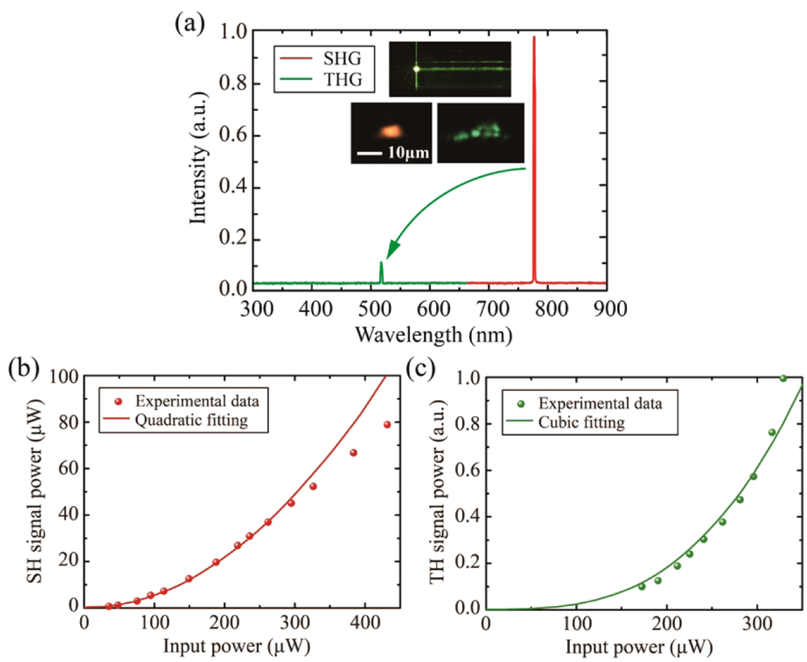

Fig. 4. SHG and cascaded THG in PPLN waveguide pumped with pulsed laser at 1556.75 nm. (a) Measured spectrum of the SHG (~778.37 nm) and THG (~518.9 nm) (not to scale). Inset: top-view of the waveguide, the mode profile of SHG (bottom left) and higher-order THG after filtering (bottom right). (b) Quadratic dependence of the output SHG power on input pulse power. (c) The normalized THG power versus the input pulse power and the corresponding cubic fitting.

Optics EXPRESS

TH (~518.9 nm) signals are observed, as shown in Fig. 4(a). The inset of Fig. 4(a) shows the image of the scattered SHG and THG from the waveguide. The THG is achieved via cascaded SHG ($\omega + \omega \rightarrow 2\omega$) and sum frequency generation (SFG) ($\omega + 2\omega \rightarrow 3\omega$). To investigate the cascade SFG mechanism, the intensity profiles of the SHG and THG at the output facet are recorded. The SHG has a fundamental mode profile (bottom left), whereas the THG possesses a higher order mode (bottom right). The cascaded process results from higher-order QPM process mixing between these different modes. Figure 4(b) reveals the output SH power varies with the input pulse power with a quadratic fitting of the experimental data. Compared with Fig. 3(b), the output SH power pumped at the non-QPM wavelength is much lower than that at the QPM wavelength under the same input pulse power. Figure 4(c) indicates the cubic dependence of THG power on the input pulse power which matches well with the theoretical expectation. Besides, we notice that the cascaded SFG process in the PPLN waveguide happens not only at the wavelength of ~1556.75 nm, but also at several other wavelengths in the QPM main lobe. However, the THG intensities at other wavelengths are extremely weak, which probably arises from phase mismatch in the cascaded SFG process.

3. Conclusion

In conclusion, we demonstrate efficient SHG and cascaded FHG at the QPM wavelength in a PPLN ridge waveguide on the LNOI platform. In addition, SHG and cascaded THG involving cascaded SFG process are also achieved at the non-QPM wavelength. Furthermore, we also report a ~62% high single-pass SHG conversion efficiency of pulsed laser. These results based on the LNOI waveguide may have potentials in integrated nonlinear frequency conversion process.

Funding. National Natural Science Foundation of China (12074252, 62022058, 62005159, 11734011) National Key Research and Development Program of China (2017YFA0303701, 2018YFA0306301); Shanghai Municipal Science and Technology Major Project (2019SHZDZX01-ZX06); Shanghai Rising-Star Program (20QA1405400); Shandong Quancheng Scholarship (00242019024);

Disclosures. The authors declare no conflicts of interest.

Data availability. Data underlying the results presented in this paper are not publicly available at this time but may be obtained from the authors upon reasonable request.

References

1. J. Wang, F. Sciarrino, A. Laing, and M. G. Thompson, "Integrated photonic quantum technologies," Nat. Photonics **14**(5), 273–284 (2020).
2. A. W. Elshaari, W. Pernice, K. Srinivasan, O. Benson, and V. Zwiller, "Hybrid integrated quantum photonic circuits," Nat. Photonics **14**(5), 285–298 (2020).
3. A. Boes, B. Corcoran, L. Chang, J. Bowers, and A. Mitchell, "Status and potential of lithium niobate on insulator (LNOI) for photonic integrated circuits," Laser Photonics Rev. **12**(4), 1700256 (2018).
4. J. T. Lin, F. Bo, Y. Cheng, and J. J. Xu, "Advances in on-chip photonic devices based on lithium niobate on insulator," Photonics Res. **8**(12), 1910–1936 (2020).
5. G. Poberaj, H. Hu, W. Sohler, and P. Gunter, "Lithium niobate on insulator (LNOI) for micro-photonic devices," Laser Photonics Rev. **6**(4), 488–503 (2012).
6. C. Wang, M. Zhang, X. Chen, M. Bertrand, A. Shams-Ansari, S. Chandrasekhar, P. Winzer, and M. Lončar, "Integrated lithium niobate electro-optic modulators operating at CMOS-compatible voltages," Nature **562**(7725), 101–104 (2018).
7. R. Baets and B. Kuyken, "High speed phase modulators for silicon photonic integrated circuits: a role for lithium niobate," Adv. Photonics **1**(03), 1 (2019).
8. M. B. He, M. Y. Xu, Y. X. Ren, J. Jian, Z. L. Ruan, Y. S. Xu, S. Q. Gao, S. H. Sun, X. Q. Wen, L. D. Zhou, L. Liu, C. J. Guo, H. Chen, S. Y. Yu, L. Liu, and X. L. Cai, "High-performance hybrid silicon and lithium niobate Mach-Zehnder modulators for 100 Gbit s^{-1} and beyond," Nat. Photonics **13**(5), 359–364 (2019).
9. C. Wang, M. Zhang, B. Stern, M. Lipson, and M. Lončar, "Nanophotonic lithium niobate electro-optic modulators," Opt. Express **26**(2), 1547–1555 (2018).
10. Z. Yu and X. Sun, "Gigahertz acousto-optic modulation and frequency shifting on etchless lithium niobate integrated platform," ACS Photonics **8**(3), 798–803 (2021).

11. M. Zhang, B. Buscaino, C. Wang, A. Shams-Ansari, C. Reimer, R. Zhu, J. M. Kahn, and M. Lončar, "Broadband electro-optic frequency comb generation in a lithium niobate microring resonator," Nature **568**(7752), 373–377 (2019).
12. C. Wang, M. Zhang, M. Yu, R. Zhu, H. Hu, and M. Lončar, "Monolithic lithium niobate photonic circuits for Kerr frequency comb generation and modulation," Nat. Commun. **10**(1), 978 (2019).
13. C. Wang, C. Langrock, A. Marandi, M. Jankowski, M. Zhang, B. Desiatov, M. M. Fejer, and M. Lončar, "Ultrahigh-efficiency wavelength conversion in nanophotonic periodically poled lithium niobate waveguides," Optica **5**(11), 1438–1441 (2018).
14. H. Jin, F. M. Liu, P. Xu, J. L. Xia, M. L. Zhong, Y. Yuan, J. W. Zhou, Y. X. Gong, W. Wang, and S. N. Zhu, "On-Chip Generation and Manipulation of Entangled Photons Based on Reconfigurable Lithium-Niobate Waveguide Circuits," Phys. Rev. Lett. **113**(10), 103601 (2014).
15. J. Zhao, C. Ma, M. Rüsing, and S. Mookherjea, "High Quality Entangled Photon Pair Generation in Periodically Poled Thin-Film Lithium Niobate Waveguides," Phys. Rev. Lett. **124**(16), 163603 (2020).
16. J. Y. Chen, C. Tang, Z. H. Ma, Z. Li, Y. M. Sua, and Y. P. Huang, "Efficient and highly tunable second-harmonic generation in Z-cut periodically poled lithium niobate nanowaveguides," Opt. Lett. **45**(13), 3789–3792 (2020).
17. L. Chang, Y. F. Li, N. Volet, L. R. Wang, J. Peters, and J. E. Bowers, "Thin film wavelength converters for photonic integrated circuits," Optica **3**(5), 531–535 (2016).
18. R. Luo, Y. He, H. Liang, M. Li, and Q. Lin, "Highly tunable efficient second-harmonic generation in a lithium niobate nanophotonic waveguide," Optica **5**(8), 1006–1011 (2018).
19. M. X. Li, H. X. Liang, R. Luo, Y. He, and Q. Lin, "High-Q 2D lithium niobate photonic crystal slab nanoresonators," Laser Photonics Rev. **13**(5), 1800228 (2019).
20. M. Li, H. Liang, R. Luo, Y. He, J. Ling, and Q. Lin, "Photon-level tuning of photonic nanocavities," Optica **6**(7), 860–863 (2019).
21. J. T. Lin, N. Yao, Z. Z. Hao, J. H. Zhang, W. B. Mao, M. Wang, W. Chu, R. B. Wu, Z. W. Fang, L. L. Qiao, W. Fang, F. Bo, and Y. Cheng, "Broadband quasi-phase-matched harmonic generation in an on-chip monocrystalline lithium niobate microdisk resonator," Phys. Rev. Lett. **122**(17), 173903 (2019).
22. R. B. Wu, J. H. Zhang, N. Yao, W. Fang, L. L. Qiao, Z. F. Chai, J. T. Lin, and Y. Cheng, "Lithium niobate micro-disk resonators of quality factors above 10^7," Opt. Lett. **43**(17), 4116–4119 (2018).
23. J. Y. Chen, Z. H. Ma, Y. M. Sua, Z. Li, C. Tang, and Y. P. Huang, "Ultra-efficient frequency conversion in quasi phase-matched lithium niobate microrings," Optica **6**(9), 1244–1245 (2019).
24. M. Zhang, C. Wang, R. Cheng, A. Shams-Ansari, and M. Loncar, "Monolithic ultra-high-Q lithium niobate microring resonator," Optica **4**(12), 1536–1537 (2017).
25. L. G. Carpenter, S. A. Berry, A. C. Gray, J. C. Gates, P. G. R. Smith, and C. B. E. Gawith, "CW demonstration of SHG spectral narrowing in a PPLN waveguide generating 2.5 W at 780 nm," Opt. Express **28**(15), 21382–21390 (2020).
26. L. G. Carpenter, S. A. Berry, R. H. S. Bannerman, A. C. Gray, and C. B. E. Gawith, "ZnO indiffused MgO: PPLN ridge waveguides," Opt. Express **27**(17), 24538–24544 (2019).
27. D. Eimerl, "High average power harmonic generation," IEEE J. Quantum Electron. **23**(5), 575–592 (1987).
28. C. Y. Cho, J. Y. Lai, C. S. Hsu, Y. T. Huang, J. H. Jang, and M. H. Chou, "Power scaling of continuous-wave second harmonic generation in a MgO:PPLN ridge waveguide and the application to a compact wavelength conversion module," Opt. Lett. **46**(12), 2852–2855 (2021).
29. B. Q. Chen, M. L. Ren, R. J. Liu, C. Zhang, Y. Sheng, B. Q. Ma, and Z. Y. Li, "Simultaneous broadband generation of second and third harmonics from chirped nonlinear photonic crystals," Light: Sci. Appl. **3**(7), e189 (2014).
30. B. Q. Chen, C. Zhang, C. Y. Hu, R. J. Liu, and Z. Y. Li, "High-efficiency broadband high-harmonic generation from a single quasi-phase-matching nonlinear crystal," Phys. Rev. Lett. **115**(8), 083902 (2015).
31. R. Wolf, I. Breunig, H. Zappe, and K. Buse, "Cascaded second-order optical nonlinearities in on-chip micro rings," Opt. Express **25**(24), 29927–29933 (2017).
32. S. J. Liu, Y. L. Zheng, Z. W. Fang, X. N. Ye, Y. Cheng, and X. F. Chen, "Effective four-wave mixing in the lithium niobate on insulator microdisk by cascading quadratic processes," Opt. Lett. **44**(6), 1456–1459 (2019).
33. T. T. Ding, Y. L. Zheng, and X. F. Chen, "Integration of cascaded electro-optic and nonlinear processes on a lithium niobate on insulator chip," Opt. Lett. **44**(6), 1524–1527 (2019).
34. M. Jankowski, C. Langrock, B. Desiatov, A. Marandi, C. Wang, M. Zhang, C. R. Phillips, M. Loncar, and M. M. Fejer, "Ultrabroadband nonlinear optics in nanophotonic periodically poled lithium niobate waveguides," Optica **7**(1), 40–46 (2020).
35. D. D. Hickstein, D. R. Carlson, A. Kowligy, M. Kirchner, S. R. Domingue, N. Nader, H. Timmers, A. Lind, G. G. Ycas, M. M. Murnane, H. C. Kapteyn, S. B. Papp, and S. A. Diddams, "High-harmonic generation in periodically poled waveguides," Optica **4**(12), 1538–1544 (2017).
36. M. Chauvet, F. Henrot, F. Bassignot, F. Devaux, L. G. Manuel, V. Pecheur, H. Maillotte, and B. Dahmani, "High efficiency frequency doubling in fully diced LiNbO3 ridge waveguides on silicon," J. Opt. **18**(8), 085503 (2016).
37. L. Ai, L. Wang, Y. Tan, S. Akhmadaliev, S. Zhou, and F. Chen, "Efficient Second Harmonic Generation of Diced Ridge Waveguides Based on Carbon Ion-Irradiated Periodically Poled LiNbO3," J. Lightwave Technol. **35**(12), 2476–2480 (2017).